Electrochemical 3D printing of copper/graphene composites with gel precursors

Journal of Manufacturing Processes 136 (2025) 18–26

Contents lists available at ScienceDirect

Journal of Manufacturing Processes

journal homepage: www.elsevier.com/locate/manpro

Electrochemical 3D printing of copper/graphene composites with gel precursors

João Paulo Coelho [1], Kaituo Zhang [1], Ren Wang, Uta Klement, Zhenyuan Xia [*]

Industrial and Materials Science, Chalmers University of Technology, Hörsalsvägen 7B, Göteborg 41296, Sweden

ARTICLE INFO

Keywords:
Electrochemical additive manufacturing
Gel precursors
Copper/graphene composite

ABSTRACT

The fusion of fashion-inspired designs with metal component production represents a significant transformation across various industries, seamlessly integrating design with functionality. While metal Additive Manufacturing (AM) has redefined the creation of customized 3D items, it encounters barriers in achieving a wider adoption due to the high investment cost. Conversely, Electrochemical Additive Manufacturing (ECAM) emerges as a promising alternative, offering cost-effectiveness and precision in fabricating metal microstructures through precise material deposition, reducing raw material waste and enabling intricate patterns without requiring expensive tooling or molds. Despite the valued properties of copper microstructures in many technological domains, their tendency to corrosion remains a severe problem. It's important to manager copper corrosion risks for preserving their functionality and durability. Copper/Graphene (Cu/Gr) composites have garnered attention for their enhanced mechanical, electrical, and thermal stability, rendering them suitable for diverse applications while also improving their anti-corrosion behavior. Herein, we explored an economical and sustainable approach to printing homogeneous Cu/Gr nanocomposites (8 mm length) using desktop ECAM coupled with cellulose-based gels as precursors. Compositional, morphological characteristics, and corrosion resistance were examined to assess their potential as electronic manufacturing components. Our findings will provide new printing strategies for metal-based nanocomposites derived from metal salts and graphene additives in aqueous solution, while also addressing the corrosion prevention to maintain the integrity and functionality of copper-based microdevices.

1. Introduction

The manufacturing of metal parts with a determined fashion design is a pivotal aspect across diverse industries, contributing to aesthetics as well as functionality [1]. In this regard, AM has transformed the process of sequential layering of materials to craft highly customized 3D items, based on digital models, with capabilities that cater to the diverse needs [2]. In spite of that, AM faces challenges in its widespread adoption and integration into existing production systems, including cost implications, stringent environmental requirements, operational overheads, and material limitations [3]. On the other hand, ECAM stands out as an emerging method that blends the principles of the traditional AM processes with Electrochemical Deposition (ECD) as a promising alternative to conventional metal AM techniques at both laboratory and industrial scales [4].

The ECAM method represents an innovative approach to manufacturing, offering numerous advantages, especially in terms of cost-effectiveness and the crafting of nano or micro-level metals and alloys [5]. It operates at lower costs primarily due to its efficient use of materials and energy [6]. Unlike metal sintering printing methods, ECAM minimizes raw material wastage by precisely depositing material onto the target substrate surface, guided by a movable nozzle [7]. This process occurs simultaneously with the migration and reduction of metal ions within an electrolyte medium, facilitating the creation of intricate patterns of layered materials on a flat base, all within a confined 3D spatial environment [8]. Moreover, the flexibility of ECAM printing eliminates the need for molds or complex masks that are often necessary in traditional electroplating process to achieve specific designs. This mask-free capability potentially reduces lowers manufacturing costs and facilitates rapid prototyping-benefits that support iterative design processes for the metal-based composite structures. Additionally, ECAM setup operates in an aqueous solution at room temperature [9,10], avoiding the thermal stresses present in other manufacturing process that could compromise the structural integrity

* Corresponding author.
E-mail address: zhenyuan@chalmers.se (Z. Xia).
[1] J. P.C. and K. Z. contributed equally to this manuscript.

https://doi.org/10.1016/j.jmapro.2025.01.055
Received 10 September 2024; Received in revised form 26 November 2024; Accepted 20 January 2025
Available online 25 January 2025

and material properties of the final product [11]. These advantages make ECAM a compelling alternative to conventional metal printing methods.

Copper is a well-known element that possesses a unique combination of thermal and electrical conductivity, along with its ductility and malleability, making it particularly easily shaped into complex structures [12]. Due to these remarkable properties, copper microstructures have found application in various technological domains, contributing to the advancement of electronic components, microelectronics, sensors, antennas, and other related fields [13]. However, despite its utility, copper microstructures are vulnerable to corrosion under certain conditions (e.g., humidity, temperature, and exposure to pollutants or corrosive substances) [14]. Furthermore, the corrosion susceptibility of a microstructured surface is intricately related to its specific geometry and features, which may lead to alterations in surface area and subsequently affecting its performance [15]. As a result, understanding and mitigating corrosion risks are essential for maintaining the functionality and longevity of copper-based microdevices and components in diverse applications. Strategies for corrosion prevention and protection may include the use of protective coatings, material selection, and environmental controls, all aimed at preserving the integrity and functionality of copper microstructures in challenging operational conditions [16].

Nowadays, composite materials, often formed by combining two or more substances with distinct chemical and physical attributes, have risen as a pathway to creating innovative materials with superior traits [17]. Within this context, the incorporation of carbon-based nanomaterials, particularly graphene, stills as a compelling option for synergetic integration with copper. Graphene, a crystalline allotrope of carbon, is distinguished by its single layer of carbon atoms arranged in a two-dimensional hexagonal lattice [18]. Each carbon atom forms covalent bonds with three adjacent carbon atoms, resulting in a robust network of sp^2 hybridized bond [19]. This unique arrangement imbues graphene with exceptional properties, including remarkable strength and flexibility [20]. In this context, Cu/Gr composite has garnered significant attention by its ability to reinforce the metal matrix [21], thereby enhancing mechanical strength [22], electrical and thermal stability [23], and anti-corrosion behavior [24], leading to more efficient electronic devices with reduced energy consumption, lightweight and durable components [25]. These qualities render Gr-based composites suitable for applications in harsh environments, as demonstrated in our recently published work [26]. Herein, we investigated a low-cost and sustainable processing route to print homogeneous microstructures based on Cu/Gr composites. The development of gel-like precursors, instead of pure water-based electrolyte solution, allows for a stable meniscus during the ECAM printing process, thereby guaranteeing a precise control of the printed Cu/Gr composites with good quality. The printed composites, with the graphene oxide (GO) content ranging from 0.1 wt% to 3.0 wt%, were examined for their compositional and morphological characteristics, as well as their resistance to corrosion as potential micro-components in a range of electronic manufacturing uses.

2. Materials and methods

2.1. Gel electrolyte preparations

The initial precursor investigations detailed herein primarily centered on two key aspects: the selection of copper ion-containing salts and the choice of appropriate thickening agents. Copper (II) nitrate (Cu$(NO_3)_2$) Copper (II) nitrate trihydrate, $Cu(NO_3)_2{\cdot}3H_2O$, ≥99 %, from Sigma Aldrich and copper (II) sulfate pentahydrate ($CuSO_4{\cdot}5H_2O$, ≥99 %, from Sigma Aldrich) were designated as primary sources of copper ions within the gel electrolyte, while polyvinyl alcohol (PVA, $(C_2H_4O)_n$, 99–100 % hydrolyzed, approx. M.W. ~124,000, from Thermo Scientific Chemicals), methyl cellulose (MC, 400 cP), and sodium carboxymethyl cellulose (CMC, average M.W. ~250,000, degree of substitution 0.7) were assessed as potential thickening agents (additional insights are available in Appendix). The ultimate compositions were determined using a concentration of 0.5 mol/L $Cu(NO_3)_2$, coupled with varying concentrations of GO ranging from 0.1 wt% to 3.0 wt% relative to the concentration of copper atoms. Additionally, four supplementary additives, including MC, H_2SO_4, poly(diallyldimethylammonium chloride) (PDDA, solution, $(C_8H_{16}ClN)_n$, 20 wt% in water, from Sigma-Aldrich), and magnesium nitrate hexahydrate ($Mg(NO_3)_2{\cdot}6H_2O$, ≥99 %, from Sigma Aldrich) were introduced in accordance with the specifications outlined in Table 1.

The process of preparing the gel electrolyte entailed gradually adding sulphuric acid into 10 mL of deionized water, copper nitrate hexahydrate, and magnesium nitrate trihydrate were followed added, and the mixture was stirred thoroughly until solution **1** was formed. After that, mixture **2** was achieved by slowly pouring 6.5 mL of absolute ethanol (C_2H_5OH, ≥99.8 %, from VWR.) to MC powder, followed by meticulous stirring using a glass rod. Subsequently, dispersion **3** was produced by pouring different quantities of GO to 10 mL of water and then subjecting it to sonication for 30 min at an amplitude of 20 % using a tip sonicator. For mixture **4**, PDDA was poured to 10 mL of water, and then underwent 30 min of sonication. Subsequently, it was combined with GO and sonicated once more under the same conditions. Mixtures **1**, **2**, and **4** were blended together to produce a gel precursor without GO. Meanwhile to form a GO-based gel precursor, mixtures **1**, **2**, **3**, and **4** were combined and diluted with water to a total volume of 50 mL. Each of the precursor materials underwent thorough stirring with a glass bar and left undisturbed until any air bubbles dissipated. Furthermore, a control precursor was prepared by mixing a specific quantity of GO with water, followed by the same sonication step, allowing it to cool to room temperature, and reserving it for further use (see Table 2).

2.2. Substrate selection

Three well-known substrates, including Copper foil (Cu, 99.99 %), highly oriented pyrolytic graphite (HOPG), and indium tin oxide (ITO) coated glass slides, underwent testing as part of this study. Therefore, ITO was selected for its favorable conductive properties and relatively flat surface compared to HOPG and Copper foil (see Figs. A3–A4).

2.3. Setup design

The configuration employed a customized industrial-grade 3D printer (ZYYX Pro, ZYYX Labs) and a direct current (DC) power supply (2260B-250-4, Keithley), as depicted in Scheme 1-left. ZYYX Labs AB crafted a syringe holder from Nylon, while a 10 mL (12 mL) syringe (5100-X00V0, Henke Sass Wolf) model was equipped with a Luer lock, suitable for deployment with an insulated nozzle (925125-DHUV, Metcal) featuring an internal diameter of 0.25 mm. Two crocodile clamps and connecting wires facilitated the connection of the anode and the stationary substrate (cathode) to the power supply, as illustrated in Scheme 1-right. The applied voltage was set at 5 V due to its widespread use, proven reliability, and the absence of electrolytic water reactions during deposition, as supported by previous studies [27]. The current was inherently constrained by the deposition process. However, as a safety precaution, the upper limit of the current was set to 0.01 mA at the power supply. To monitor the current and resistance of the wire between the anode/cathode and the power supply, a digital multimeter (DMM) model 175 True-RMS by Fluke was utilized.

Table 1
Selected additives for the gel electrolyte composition.

Additive	Concentration	Function
MC	25 g/L	To increase viscosity
H_2SO_4	0.1 mol/L	To increase ionic conductivity
PDDA	3:8 to GO	To improve GO dispersion
$Mg(NO_3)_2$	1:1 to GO	To adjust surface charge of GO

Table 2
Formulation of the gel electrolytes for ECAM printing.

Sample	$Cu(NO_3)_2$ (mL)	H_2SO_4 (mol/L)	MC (g/L)	GO (mL)	PDDA (g/L)	$Mg(NO_3)_2$ (g/L)
Pure-Cu	0.50	0.10	25.00	–	0.10	0.32
Cu/0.1GO	0.50	0.10	25.00	0.40	0.01	0.03
Cu/0.5GO	0.50	0.10	25.00	2.00	0.06	0.16
Cu/1.0GO	0.50	0.10	25.00	4.00	0.12	0.32
Cu/2.0GO	0.50	0.10	25.00	8.00	0.24	0.64
Cu/3.0GO	0.50	0.10	25.00	12.00	0.36	0.96
3.0GO@Cu	–	–	–	12.00	–	–

2.4. Programming

Initially, a computer-aided design (CAD) model was utilized to be crafted and then converted into a standard triangle language (STL) file format. The geometric code (G-code), a machine-executable language, was generated and inputted into the 3D printer using Simplify3D software. Consequently, the enclosed ECD system initiates material deposition in a predetermined shape onto the target substrate. The distance between the nozzle and the substrate surface, known as the fly-height, could be modified either through computer software or by physically adjusting the position of the syringe in the Z direction. The pattern was designed to produce a single straight line measuring 8 mm in length. The speed of nozzle movement was set to 1 mm/s, ensuring precise and controlled material deposition. With this configuration, the total printing time for the project amounted to 30 min. The fly-height was maintained within the range of 100 to 200 μm throughout the printing process, ensuring optimal printing conditions and layer adhesion.

2.5. Manufacturing procedure

All experiments were conducted at ambient temperature, with careful attention to ensure the cleanliness of laboratory equipment, particularly conductive substrates, nozzles, syringes, and tools. These items underwent thorough cleaning both before and after use, successively with ethanol followed by water rinsing. The extensive procedure of ECAM involved thorough cleaning and sonication of anodes with acetone, ethanol, and water, followed by washing with a solution containing 40 % H_2SO_4 (97 %, from Supelco), 20 % HNO_3 (65 % from Supelco), 0.2 % HCl (37 %, from Supelco), and deionized water. The conductive base was affixed to the platform of the printer using conductive copper tape (1136, 3 M), while a simple connector was used to link the negative terminal of the power supply, as depicted in Scheme 1. The nozzle and syringe were assembled and securely attached to the syringe holder. Two milliliters of the pre-prepared gel electrolyte were loaded, and the anode was inserted into the nozzle, connecting it to the positive terminal of the power supply utilizing a crocodile clamp. Printing was initiated either via the printer control panel or the computer interface. Following the printing of three layers, a few drops of benzotriazole (BTA, $C_6H_5N_3$, 99 %, from Sigma Aldrich) solution (1 mmol/L) were applied onto the deposition surface, according to the printing area requirements. This procedure was implemented to prevent excessive drying of the gel electrolyte, thus reducing the risk of nozzle blockage and potential damage to the deposited components. Upon completion of the printing process, the sample, along with the substrate, was taken off from the platform and cleansed using a BTA solution. Subsequently, it was soaked in a BTA solution for a duration of 10 min followed by a vacuum oven (Glass Oven B-585, Buchi) at a temperature of 40 °C. To prepare the control sample (3.0GO@Cu), a copper foil was sequentially washed with acetone, ethanol, and water. Then, graphene oxide (water dispersion, 0.4 wt%, from Graphenea) was drop casted onto the cleaned surface of copper foil, and dried in a vacuum oven at 40 °C.

2.6. Characterization of the microstructures

In this study, the pure-Cu sample served as the reference material, and the chosen techniques for analyzing the deposited samples were intended to address three primary objectives: examining changes in the surface morphology subsequent to the addition of GO to copper deposition, observing the distribution of GO and potential presence of reduced graphene oxide (rGO) resulting from electrochemical reduction, and investigating possible applications of the samples in energy storage. To achieve this, a combination of SEM (Scanning Electron Microscopy), Raman spectroscopy, XPS (X-ray Photoelectron Spectroscopy), CV (cyclic voltammetry), and anti-corrosion testing methods were employed.

SEM imaging was conducted with a JEOL JSM-7800F Prime instrument to analyze the surface morphology and cross-sectional thickness of each sample. The acceleration voltage during testing was adjusted within the range of 2 kV to 5 kV while operating under secondary electron mode. A LED detector was selected, and a working distance of 10.4 mm was upheld to ensure optimal imaging. Raman analysis, utilizing a WITec alpha300 R instrument, was performed in order to verify the dispersion of moieties derived from graphene. The laser source was adjusted to $\lambda_{ex} = 532$ nm, and a power output of 1.0 mW. Single-point spectra and mapping outcomes were recorded at 100× magnification employing Optical Microscopy (OM) with an aperture of 0.9. The scanning XPS microprobe utilized for the analysis was the PHI5000 VersaProbe III, equipped with a monochromatic Aluminum (Al) Kα X-ray source boasting an energy of 1486.6 eV. The bean diameter was adjusted to 100 μm, with a power output of 25 W and a voltage of 15 kV.

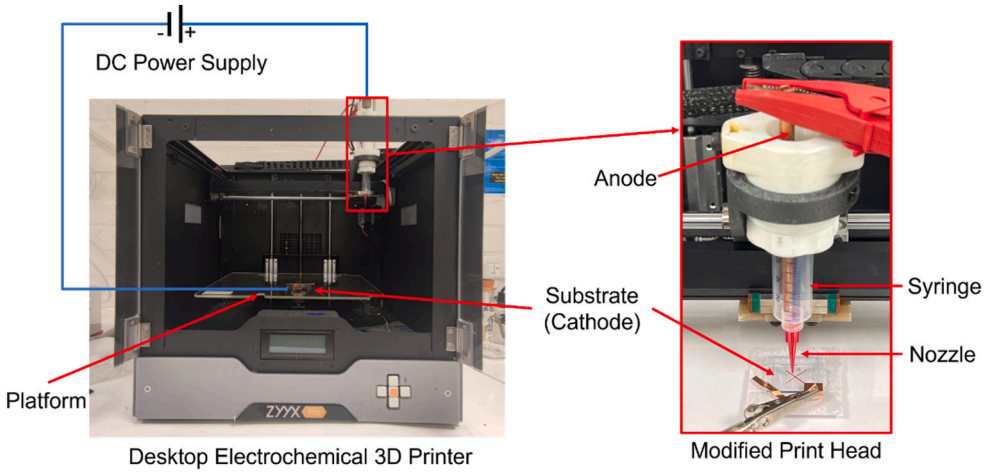

Scheme 1. The modified desktop 3D printer (left) and its print head (right).

Two scanning modes were implemented: an initial survey scan covering the energy range from 0 to 1300 eV with a step increment of 1.00 eV, to comprehensively assess the sample composition; and a narrow scan performed in specific regions of interest to scrutinize the chemical state. The increment size was adjusted to 0.05 eV for the C1s element, contrasting with the 0.10 eV set for other elements. The energy resolution of 0.654 eV was attained with a 100 μm beam, as indicated by the full width at half maximum. Calibration of narrow scan measurements was conducted to precisely coincide with the graphitic carbon peak (C1s) at 284.6 eV, ensuring an accurate level of analysis. The minimal detectable concentration for this XPS setup was established at 1.0 at.%, underlining its reliable capability to identify elements at concentrations above this threshold. The CV assessment was performed using a Bio-Logic SP-300 electrochemistry workstation, with each sample undergoing three cycles of testing. Voltage scanning ranged from −0.5 V to 0 V, and 0 V to 0.5 V at a rate of 100 mV/s. A three-electrode system was utilized, comprising a 5 mm^2 working electrode (WE), a counter electrode (CE) composed of 99.99 % platinum (Pt), and a reference electrode (RE) - Ag/AgCl/KCl (saturated). Tests to assess the corrosion resistance of Cu/GO-based composites under conditions resembling seawater, utilizing aerated 3.5 % sodium chloride (NaCl, ≥99,8 %, from VWR) solution at pH 7, as opposed to the solution utilized in CV assessments. The evaluation method employed linear polarization resistance (LPR), adhering to ASTM-G59 standards. The rate of voltage change was set at 1 mV/s, initiating at −1 V in relation to the reference electrode. Each test consisted of a step increment of 25 %, repeated five times, covering a measurement range from −1 V to 1 V, current range was set to 10 mA with a bandwidth of 7.

3. Results and discussions

3.1. Surface morphology

The surface observation was conducted on six samples, including pure-Cu and various Cu/GO composites, each with a thickness of ~10–20 μm, using a scanning electron microscope (SEM) set at a magnification of 100× (Figs. 1 and A5). Upon examination, it was noted that with the increasing content of GO, there was a corresponding enhancement in surface smoothness across all the samples. The addition of GO to the composite structure also introduced a more intricate surface matrix, with occasional voids and micro-cracks in samples with GO content above 0.5 % [28]. However, these features did not compromise the overall integrity and the following anticorrosion behavior of the composites. In addition, samples with GO content ≥0.5 % exhibited observable uneven growth on both boundaries. While jagged edges were more prominent in lines with GO content below 0.5 %, their roughness level was less noticeable. Uniformly distributed dark spots, protruding from the surface, were also detected across all samples. These spots are likely due to the accelerated oxidation of copper in raised areas compared to the flat regions, particularly evident during storage periods [29]. As illustrated in Fig. 1-insets, the surface of pure-Cu displays distinct hemispheres features, while the incorporation of GO results in the formation of hilly-like protrusions on the surface. Remarkably, Cu/3.0 GO demonstrates an overall smooth surface with more pronounced cracks. The incorporation of GO contributes to a smoother surface of deposits, however, there is no apparent trend concerning the various GO contents.

The structural analysis indicates that both the hemispherical shape of pure-Cu and the rippled patterns of Cu/GO samples unveiled the presence of copper crystals. However, a notable contrast arises in the size of these crystals, which undergoes variation upon the introduction of GO into the initial substances [30]. Pure-Cu displays a copper crystal size of roughly 0.5 μm, whereas GO-containing samples exhibit a crystal size at least twice as large. GO or rGO presence was not apparent on the surface. Moreover, SEM inspections revealed that when magnification resolutions surpass 20,000×, the surface becomes blurred. This occurrence can be attributed to the post-treatment application of BTA, which leads to the formation of a non-conductive BTA layer on the surface of the deposit due to precipitation. Consequently, this thin layer disrupts the electron signal observed during SEM analyses [31].

3.2. Composition distribution

Upon analyzing the Raman mapping outcomes, as depicted in Fig. 2, it becomes evident that the overall concentration of graphene-related materials progressive rises with the GO content in the precursor [32].

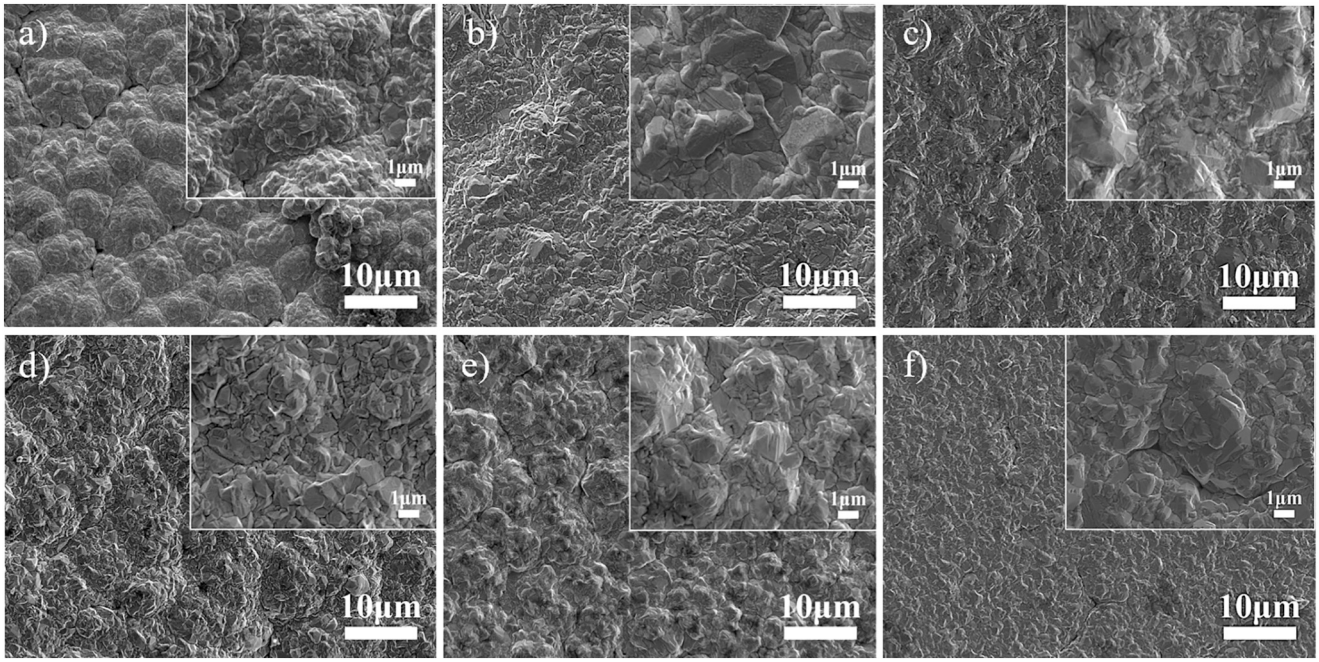

Fig. 1. SEM micrographs (2000×) of pure Cu (a), Cu/0.1GO (b), Cu/0.5GO (c), Cu/1.0GO (d), Cu/2.0GO (e), and Cu/3.0GO (f) samples, and correspondent SEM images (20.000×) in the insets.

Moreover, the dispersion of these graphene-related materials exhibits a higher level of uniformity. A thorough examination was conducted on all specimens to pinpoint areas containing graphene-related materials, and the outcomes are detailed in Fig. 2. These results highlight the presence of GO and/or rGO. Particularly, the prominence and close alignment of the intensities of the D band (≈1354 cm^{-1}) and G band (≈1603 cm^{-1}) [33]. The G band is a special feature of carbon-based materials such as graphite, carbon nanotubes and graphene [34]. It originates from the in-plane of carbon atoms, specifically from the E2g mode associated with the sp^2 hybridization [35]. Conversely, the D band is another characteristic aspect which is linked in-plane imperfections or defects from graphitic lattice vibration [36]. This band is often associated with defects and disorders within the carbon lattice such as vacancies, grain boundaries, or edges [37]. These bands were observed in all GO and/or rGO containing samples except in pure-Cu. Furthermore, the intensity ratios of the D band and G band, referred to as I_D/I_G, vary between 0.98 and 1.07, as depicted in Fig. 3. This I_D/I_G ratio can provide valuable insights into the degree of disorder or crystallinity present in the materials [38].

Both, Raman mapping and spectra analyses, reveal that the distribution of GO/rGO across the sample surface increases proportionally with higher GO composition in the precursor. The I_D/I_G ratio, obtained for all investigated cases, approaches a unity for graphene, which suggests the presence of defects. These structural disorders stem from the oxidation reactions that introduced oxygen atoms to the graphene framework, resulting in the formation of oxygenated groups such as hydroxyl (—OH), epoxy (—O—), carboxyl (—COOH), etc. [39]. The XPS spectral data below provides supplementary evidence corroborating the presence of GO.

Fig. 4a shows the XPS survey spectra from two samples, Cu/3.0GO and 3.0GO@Cu, disclosing elemental compositions and bonding environments. Both samples are primarily composed of carbon (C) and oxygen (O), as anticipated. Minor traces of nitrogen (N) and Cu were observed in Cu/3.0GO, whereas traces of sulfur (S) and Cu were found in 3.0GO@Cu. Figs. 4b–6e present detailed deconvolution XPS spectra of the C1s and O1s regions. In both samples, the C1s spectra revealed four component peaks at 284.6 eV, 286.5 eV, and 288.0 eV, which refer to C—C (sp^2 C bond), C—O, and O—C—O, respectively. Likewise, the O1s spectra exhibited two component bands indicative of characteristic oxygen bonds at 531.0 eV and 532.6 eV, corresponding to C═O and C—O structure [40].

Table 3 provides details on the binding energies, corresponding chemical bonds, and the percentage distribution of bonds derived from C1s and O1s XPS spectra.

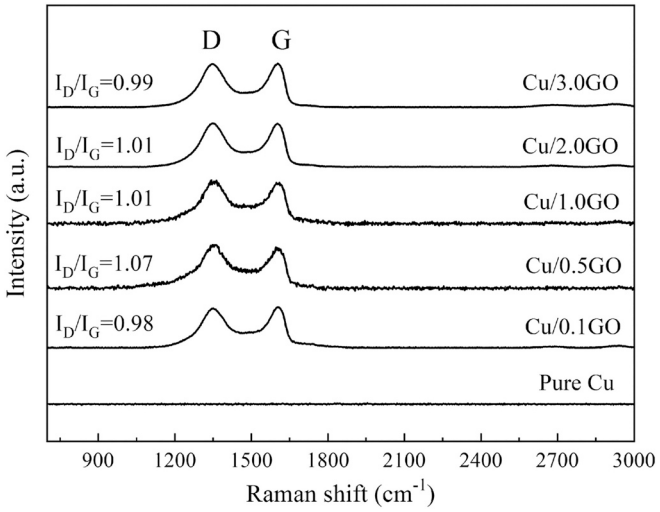

Fig. 3. Raman spectra of samples showing the variation of I_D/I_G ratios according to distinct GO contents present in the investigated samples.

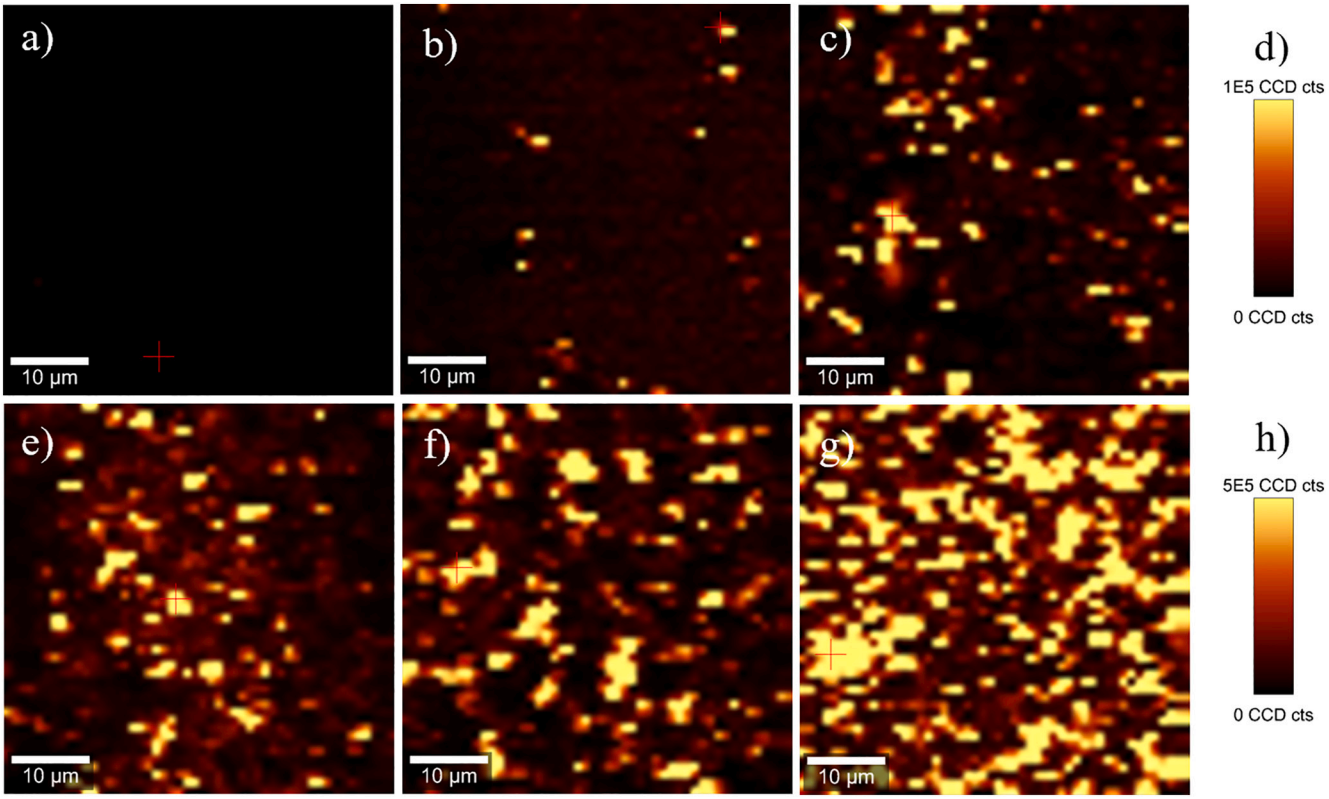

Fig. 2. Raman mapping of pure Cu (a), Cu/0.1GO (b), and Cu/0.5GO (c), refer to the scale in (d), Cu/1.0GO (e), Cu/2.0GO (f), and Cu/3.0GO (g), refer to the scale in (h).

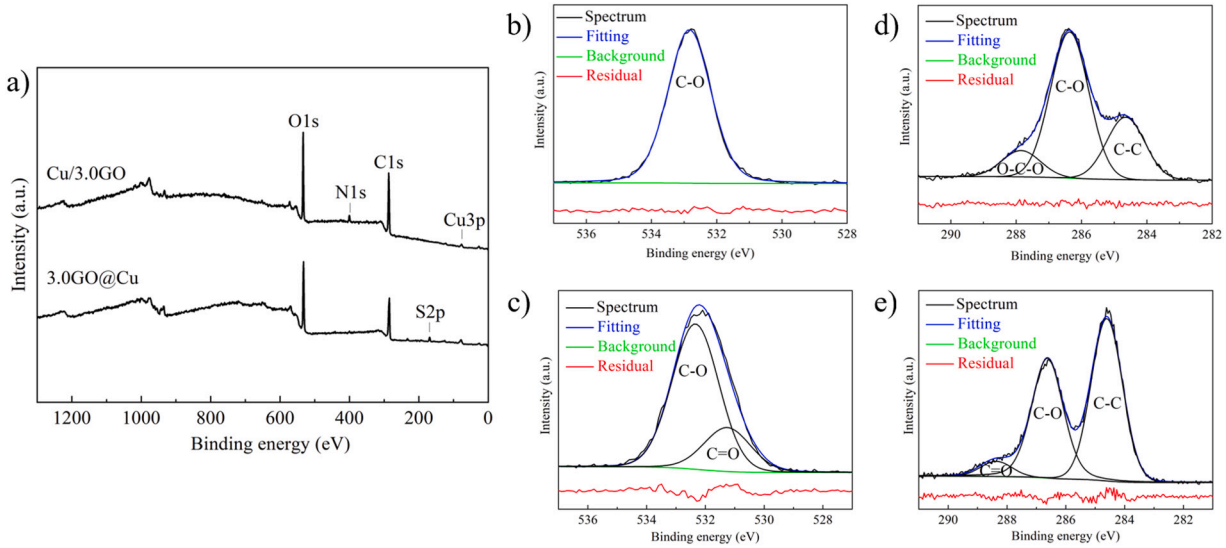

Fig. 4. XPS survey spectra (a), deconvoluted XPS spectra of C1s region from Cu/3.0GO and 3.0GO@Cu (b and c, respectively) and O1s region from Cu/3.0GO and 3.0GO@Cu (c and d, respectively).

The C and O atomic concentrations were quantified by the XPS measurements as outlined in Table 4. The carbon levels remained fairly stable for both samples, Cu/3.0GO and 3.0GO@Cu, hovering around 60.5 at.% and 63.0 at.%, respectively. The presence of oxygen was observed at levels of about 34.5 at.% in Cu/3.0GO and 32.0 at.% in 3.0GO@Cu. The proportion of sp^2 C bonds (i.e. C1s = 284.6 eV, C—C) in Cu/3.0GO decreased to 16.5 at.%, contrasting with 32.0 at.% in 3.0GO@Cu. Moreover, the carbon-to-oxygen atom ratios (C/O), determined through XPS analysis, were calculated as 1.75 for Cu/3.0GO and 1.97 for 3.0GO@Cu. These findings suggest a reduction in the content of the C—C (sp^2) bonds and an increase in the C—O content post-deposition [41]. However, the overall carbon and oxygen content remains relatively stable. Furthermore, both samples exhibit a predominance of carbon and oxygen, with minor amounts of copper (Fig. 4a). It is hypothesized that the variation in sp^2 C-bond content could be attributed to the addition of PDDA or BTA, or possibly impurities during the processing stages.

3.3. Electrochemical properties

The assessment of electrochemical behavior comprised two distinct segments. Initially, the deposits underwent a CV test to examine their electrochemical behavior and their responsiveness to interact with substances within the solution via electrochemical activity, redox reaction, and their associated mechanism. In the subsequent section, the focus shifted to evaluating the corrosion tendencies of pure-Cu and identifying any potential improvements in resistance associated with the Cu/GO composites.

The obtained CV results for pure-Cu and composite samples are shown in Fig. 5a. The transition between different oxidation states of copper, specifically Cu^+/Cu [42], was detected across all samples along the anodic scan within the voltage range from −0.5 to 0 V, at a scan rate of 100 mV/s. Meanwhile, oxidation peaks, signaling reduction, were observed within the −0.3 to −0.2 V range in all cases. Despite similar shapes, variations in their current density and potential were observed among the samples. The addition of GO caused a shift of the cathodic peak to the left [43], indicating changes in the reduction processes occurring at lower voltages compared to the pure-Cu. In this case, the potential shifted from −0.20 V to approximately −0.27 V (range from −0.25 to −0.30 V) for samples in the presence of GO. The absence of a reduction peak suggests that the samples underwent an irreversible reaction when used as a working electrode. Significantly, the presence of GO assisted in delaying the oxidation of copper [44]. Subsequently, $Cu^{+/}$Cu redox couple was analyzed by a CV scan covering a voltage range of 0 to 0.5 V, maintaining the same scan rate as before, as shown in Fig. 5b. Distinct anodic peaks are observed around 0.35 V, indicating a reduction in all samples, except for Cu/1.0GO which displayed a peak closer to 0.4 V, under varied current densities ranging between 200 and 470 mA/cm^2. Moreover, the absence of oxidation peaks suggests an irreversible reaction, as indicated by the CV findings. In this case, the presence of GO seemed to have minimal influence on the reduction reaction. Additionally, the established mechanism of copper dissolution in (Cl^-) solutions, i.e. 1 mol/L KCl, as outlined in Eqs. (1) and (2), provides insights into its behavior during oxidation or reduction reactions.

Table 3
XPS chemical state analysis of Cu/3.0GO and 3.0GO@Cu.

	C1s				O1s	
Binding energy (eV)	284.6	286.5	288.0	288.5	531.0	532.6
Bond type	C—C (sp^2)	C—O	O—C—O	C═O	C═O	C—O
Cu/3.0GO	16.5 %	39.0 %	7.5 %	–	–	33.5 %
3.0GO@Cu	32.0 %	25.5 %	–	3.0 %	8.5 %	26.0 %

Table 4
Surface composition of Cu/3.0GO and 3.0GO@Cu from XPS.

Sample	C (at.%)	O (at.%)	Cu (at.%)
Cu/3.0GO	60.5	34.5	3.0
3.0GO@Cu	63.0	32.0	1.5

$$Cu + Cl^- \leftrightarrow CuCl + e^- \quad (1)$$

$$CuCl + Cl^- \leftrightarrow CuCl_2^- \quad (2)$$

Copper immersed in a solution containing Cl^- ions undergoes dissolution, yielding Cu^+ ions, specifically $CuCl_2^-$, which is a thermodynamically stable complex [45]. Moreover, no evidence of a reduction reaction involving GO is observed in either of the CV diagrams, indicating the stability of GO within these composites.

The electrochemical corrosion performance of the samples was assessed through LPR testing, as depicted in Fig. 6, whereas Tafel

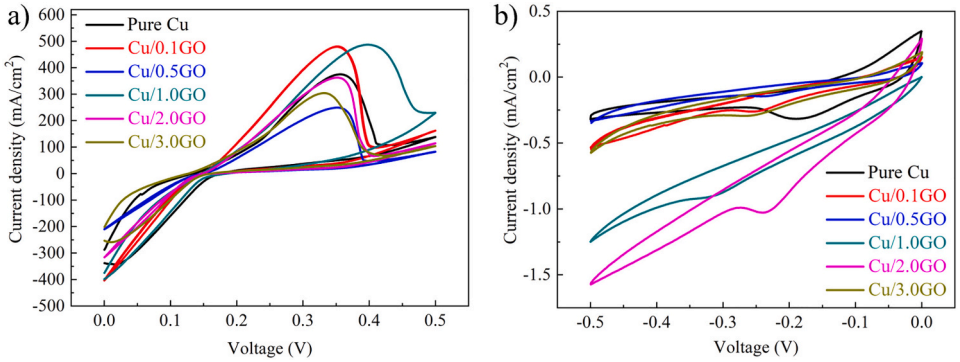

Fig. 5. Cyclic voltammetry curves for pure-Cu and composites at room temperature.

polarization fittings were utilized to determine the corrosion parameters such as corrosion current density (i_{corr}) and Tafel slopes β_a and β_c (for anodic and cathodic reactions, respectively), as summarized in Table 5. The self-corrosive potential for pure-Cu was utilized as a control, set at −0.08 V, to evaluate the LPR curve. It was noted that samples with elevated concentrations of GO, such as Cu/1.0GO, Cu/2.0GO, and Cu/3.0GO, exhibited higher self-corrosive potentials. More precisely, their values were recorded as −0.184 V, −0.192 V, and −0.203 V, respectively. Conversely, samples with lower concentrations of GO exhibited lower potentials, registering −0.151 V for Cu/0.1GO and −0.159 V for Cu/0.5GO. In terms of current density, only Cu/3.0GO −172 mA/cm^2, while the others maintain values near −200 mA/cm^2.

For a thorough understanding of the impact of GO doping and its quantification, the corrosion inhibition efficiency (*IE*) [46] was calculated using Eq. (3).

$$IE = \frac{i^0_{corr-i_{corr}}}{i^0_{corr}} \times 100\% \quad (3)$$

In the equation context, i^0_{corr} and i_{corr} denote the corrosion current density of pure-Cu and Cu/GO composites electrodes, correspondingly, and Table 5 presents the corrosion inhibition efficiency (*IE*) values. These findings suggest that although there are fluctuations in the E_{corr} values among different samples with varying GO concentrations [47], there is a notable reduction in i_{corr} for Cu/GO composites, ranging from 5.048 to 8.766 mA/cm^2, in contrast to the value of 88.184 mA/cm^2 for pure-Cu. This decrease in values implies an improvement in corrosion resistance with the incorporation of GO. Furthermore, the consistently positive *IE* values from Cu/GO samples indicate an effective corrosion reduction compared to the control.

Table 5
Comparative electrochemical corrosion values for pure-Cu and composites.

Sample	β_c (mV)	B_a (mV)	E_{corr} (mV)	i_{corr} (mA/cm^2)	*IE* (%)
Pure-Cu	235.6	208.7	−198.327	88.184	–
Cu/0.1GO	72.1	56.9	−176.592	6.631	92.48
Cu/0.5GO	80.0	88.3	−143.548	5.048	94.27
Cu/1.0GO	89.4	66.4	−149.834	6.229	92.93
Cu/2.0GO	89.3	87.3	−187.453	7.091	91.95
Cu/3.0GO	85.5	56.5	−176.233	8.766	90.05

A comprehensive understanding of the corrosion behavior and the effectiveness of GO in improving corrosion resistance was acquired by assessing both polarization results and Tafel fitting analyses. However, the relationship between GO content and corrosion improvement may not be straightforward, potentially due to other factors such as the presence of the BTA film and variations in surface characteristics among samples. Previous research has emphasized the critical role of surface features in shaping corrosion resistance [48]. Imperfections such as roughness, voids, and cracks have been directly related in expediting the oxidation process of copper [49], thereby compromising its corrosion performance.

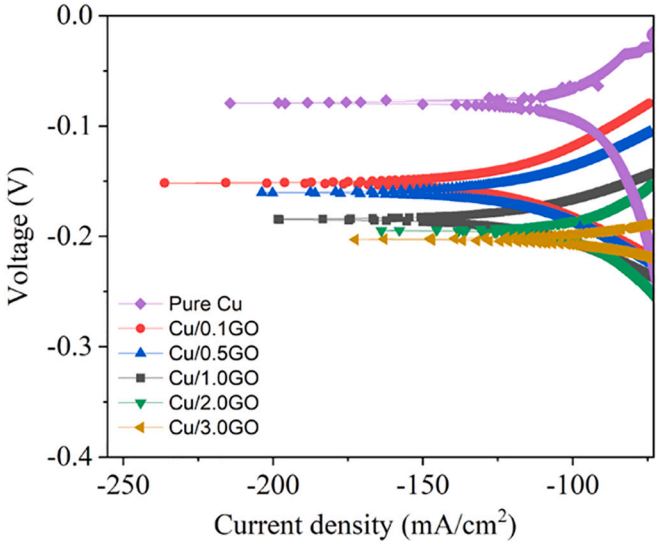

Fig. 6. LPR curves obtained from samples with distinct GO contents.

4. Conclusions

In this work, we optimized electrolyte solutions containing $Cu(NO_3)_2$ and GO in various concentrations, incorporating appropriate additives such as PDDA, along with a thickener (MC), to formulate a solution suitable for printing 8-mm-length microstructures onto ITO substrate via ECAM method at room temperature. Morphological analysis showed that increasing GO content improved surface smoothness and flatness but led to the appearance of defects such as cracks and voids. Composition examination revealed a gradual rise in the overall concentration of graphene-related materials with increasing GO content in the precursor, supported by the analysis of the ID/IG intensities of the D band and G, which varied from 0.98 to 1.07. XPS analysis indicated atomic concentrations of C (60.5 %), O (34.5 %), and Cu (3 %) for the Cu/3.0GO sample. Electrochemical properties demonstrated that the GO addition affected CU oxidation behavior, delaying oxidation without significantly impacting the reduction reaction. Moreover, the anti-corrosion tests suggested that the GO-added deposits reduced the current density from 90 % to 94 % in comparison with the control sample. Therefore, the utilization of a customized printer alongside laboratory facilities showcased an efficient approach to manufacturing metal parts for a diverse technological purpose.

CRediT authorship contribution statement

João Paulo Coelho: Writing – review & editing, Writing – original draft. **Kaituo Zhang:** Validation, Methodology, Investigation. **Ren Wang:** Validation, Investigation, Data curation. **Uta Klement:** Supervision, Funding acquisition. **Zhenyuan Xia:** Writing – review & editing, Supervision, Funding acquisition, Conceptualization.

Funding

This work has been funded by the VINNOVA (project GO–FOR–WATER 2019-05353), the Swedish Innovation Agency, and the Swedish Åforsk Foundation, project (no. 222–263) is gratefully acknowledged.

Declaration of competing interest

The authors declare that they have no known competing financial interests or personal relationships that could have appeared to influence the work reported in this paper.

Acknowledgements

João Paulo Coelho acknowledges the fellowship received from the Conselho Nacional de Desenvolvimento Científico e Tecnológico (CNPq) of the Ministério da Ciência e Tecnologia e Inovações (MCTI), as well as the support from the Centro de Pesquisa e Inovação Sueco-Brasileiro (CISB) and Saab AB.

Appendix A. Supplementary data

Supplementary data to this article can be found online at https://doi.org/10.1016/j.jmapro.2025.01.055.

References

[1] Kumar A. Methods and materials for smart manufacturing: additive manufacturing, internet of things, flexible sensors and soft robotics. Manuf Lett 2018;15:122–5. https://doi.org/10.1016/j.mfglet.2017.12.014.
[2] Mehrpouya M, Dehghanghadikolaei A, Fotovvati B, Vosooghnia A, Emamian SS, Gisario A. The potential of additive manufacturing in the smart factory industrial 4.0: a review. Appl Sci 2019;9:3865. https://doi.org/10.3390/app9183865.
[3] Jung S, Kara LB, Nie Z, Simpson TW, Whitefoot KS. Is additive manufacturing an environmentally and economically preferred alternative for mass production? Environ Sci Technol 2023;16:6373–86. https://doi.org/10.1021/acs.est.2c04927.
[4] Hengsteler J, Kanes KA, Khasanova L, Momotenko D. Beginner's guide to micro- and nanoscale electrochemical additive manufacturing. Annu Rev Anal Chem 2023;16:71–91. https://doi.org/10.1146/annurev-anchem-091522-122334.
[5] Crapnell RD, Kalinke C, Silva LRG, Stefano JS, Williams RJ, Munoz RAA, et al. Additive manufacturing electrochemistry: an overview of producing bespoke conductive additive manufacturing filaments. Mater Today 2023;71:73–90. https://doi.org/10.1016/j.mattod.2023.11.002.
[6] Li X, Ming P, Ao S, Wang W. Review of additive electrochemical micro-manufacturing technology. Int J Mach Tool Manuf 2022;173:103848. https://doi.org/10.1016/j.ijmachtools.2021.103848.
[7] Kim Y, Kang D, Kim H, Kim S, Yoo B. The characteristics of selective 3D metal additive process using electrochemical deposition and nozzle fluid dynamics. Fron Mech Eng 2020;6. https://doi.org/10.3389/fmech.2020.00009.
[8] Siddiqui H, Singh N, Katiyar D, Naidu P, Mishra S, Prasad HC, et al. Electrochemical additive manufacturing (ECAM): a new approach to fabricate metal nanostructures. Mater Today: Proc 2023;72:2741–8. https://doi.org/10.1016/j.matpr.2022.09.513.
[9] Huang Z, Shao G, Li L. Micro/nano functional devices fabricated by additive manufacturing. Prog Mater Sci 2023;131:101020. https://doi.org/10.1016/j.pmatsci.2022.101020.
[10] Chen X, Liu X, Childs P, Brandon N, Wu B. A low-cost desktop electrochemical metal 3D printer. Adv Mater Technol 2017;2:1700148. https://doi.org/10.1002/admt.201700148.
[11] Ladd C, So JH, Muth J, Dickey MD. 3D printing of free-standing liquid metal microstructures. Adv Mater 2013;25:5081–5. https://doi.org/10.1002/adma.201301400.
[12] Yang HY, Ma ZC, Lei CH, Meng L, Fang YT, Liu JB, et al. High strength and high conductivity Cu alloys: a review. Sci China Technol Sci 2020;63:2505–17. https://doi.org/10.1007/s11431-020-1633-8.
[13] Lai Z, Mai Y, Song H, Mai J, Jie X. Heterogeneous microstructure enables a synergy of strength, ductility and electrical conductivity in copper alloys. J Alloys Compd 2022;902:163646. https://doi.org/10.1016/j.jallcom.2022.163646.
[14] Lombardia EM, Lapeire L, De Graeve I, Verbeken K, Kestens LAI, Terryn H. Study of the influence of the microstructure on the corrosion properties of pure copper. Mater Corros 2016;67:847–56. https://doi.org/10.1002/maco.201508719.
[15] Wu B, Ibrahim MZ, Raja S, Yusof F, Razak BBA, Muhamad MRB, et al. The influence of reinforcement particles friction stir processing on microstructure, mechanical properties, tribological and corrosion behaviors: a review. J Mater Res Technol 2022;20:1940–75. https://doi.org/10.1016/j.jmrt.2022.07.172.
[16] Chen S, Chen Y, Lei Y, Yin Y. Novel strategy in enhancing stability and corrosion resistance for hydrophobic functional films on copper surfaces. Electrochem Commun 2009;11:1675–9. https://doi.org/10.1016/j.elecom.2009.06.021.
[17] Hasan M, Zhao J, Jiang Z. Micromanufacturing of composite materials: a review. Int J Extrem Manuf 2019;1:012004. https://doi.org/10.1088/2631-7990/ab0f74.
[18] Ares P, Novoselov KS. Recent advances in graphene and other 2D materials. Nano Mater Sci 2021;4:3–9. https://doi.org/10.1016/j.nanoms.2021.05.002.
[19] Wang JT, Qian Y, Weng H, Wang E, Chen C. Three-dimensional crystalline modification of graphene in all-sp2 hexagonal lattices with or without topological nodal lines. J Phys Chem Lett 2019;10:2515–21. https://doi.org/10.1021/acs.jpclett.9b00844.
[20] Zhou T, Cheng Q. Chemical strategies for making strong graphene materials. Angew Chem Int Ed 2021;60:18397–410. https://doi.org/10.1002/anie.202102761.
[21] Palermo V, Kinloch IA, Ligi S, Pugno NM. Nanoscale mechanics of graphene and graphene oxide in composites: a scientific and technological perspective. Adv Mater 2016;28:6232–8. https://doi.org/10.1002/adma.201505469.
[22] Gao J, Zhou M, Cheng G, Tang M, Sun L, Chen Y, et al. Multilayer coatings of periodically co-deposited graphene and ag substrate: improving the electrified friction interface by modifying the strength-ductility combination. Surf Coat Technol 2024;482:130667. https://doi.org/10.1016/j.surfcoat.2024.130667.
[23] Huang Z, Wang C, Zhou L, Wu C. Thermal conductivity enhancement and shape stability of phase-change materials using high-strength 3D graphene skeleton. Surf Interfaces 2021;26:101338. https://doi.org/10.1016/j.surfin.2021.101338.
[24] Sun J, Martinsen KH, Klement U, Kovtun A, Xia Z, Silva PFB, et al. Controllable coating graphene oxide and silanes on cu particles as dual protection for anticorrosion. ACS Appl Mater Interfaces 2023;15:38857–66. https://doi.org/10.1021/acsami.3c08042.
[25] Zhao Z, Bai P, Du W, Liu B, Pan D, Das R, et al. An overview of graphene and its derivatives reinforced metal matrix composites: preparation, properties and applications. Carbon 2020;170:302–26. https://doi.org/10.1016/j.carbon.2020.08.040.
[26] Mulone A, Xia Z, Klement U. Electrodeposition of FeW-graphene composites: effect of graphene oxide concentration on microstructure, hardness and corrosion properties. Flatchem 2023;40:100525. https://doi.org/10.1016/j.flatc.2023.100525.
[27] Heitz E. Corrosion of metals in organic solvents. Adv Corros Sci Technol 1974;4:149–243. https://doi.org/10.1007/978-1-4615-9059-0_3.
[28] Yang Z, Wang L, Shi Z, Wang M, Cui Y, Wei B, et al. Preparation mechanism of hierarchical layered structure of graphene/copper composite with ultrahigh tensile strength. Carbon 2018;127:329–39. https://doi.org/10.1016/j.carbon.2017.10.095.
[29] Avcu E, Cao H, Zhang X, Guo Y, Withers PJ, Li X, et al. The effect of reduced graphene oxide content on the microstructural and mechanical properties of copper metal matrix composites. Mater Sci Eng A 2022;856:143921. https://doi.org/10.1016/j.msea.2022.143921.
[30] Zhan K, Wang W, Li F, Cao J, Liu J, Yang Z, et al. Microstructure and properties of graphene oxide reinforced copper-matrix composite foils fabricated by ultrasonic assisted electrodeposition. Mater Sci Eng A 2023;872:144995. https://doi.org/10.1016/j.msea.2023.144995.
[31] Brusic V, Frankel GS, Roldan J, Saraf R. Corrosion and protection of a conductive silver paste. J Electrochem Soc 1995;142:2591. https://doi.org/10.1149/1.2050058.
[32] Sun Y, Sun J, Sanchez JS, Xia Z, Xiao L, Chen R, et al. Surface chemistry and structure manipulation of graphene-related materials to address the challenges of electrochemical energy storage. Chem Commun 2023;59:2571–83. https://doi.org/10.1039/D2CC06772B.
[33] Saito R, Hofmann M, Dresselhaus G, Jorio A, Dresselhaus MS. Raman spectroscopy of graphene and carbon nanotubes. Adv Phys 2011;60:413–550. https://doi.org/10.1080/00018732.2011.582251.
[34] Jorio A, Dresselhaus MS, Saito R, Dresselhaus G. Raman spectroscopy in graphene related systems. John Wiley & Sons; 2011. https://doi.org/10.1002/9783527632695.
[35] Ferrari AC. Solid State Commun 2007;143:47–57. https://doi.org/10.1016/j.ssc.2007.03.052.
[36] Lee AY, Yang K, Anh ND, Park C, Lee SM, Lee TG, et al. Raman study of D* band in graphene oxide and its correlation with reduction. Appl Surf Sci 2021;536:147990. https://doi.org/10.1016/j.apsusc.2020.147990.
[37] Wu JB, Lin ML, Cong X, Liu HN, Tan PH. Raman spectroscopy of graphene-based materials and its applications in related devices. Chem Soc Rev 2018;47:1822–73. https://doi.org/10.1039/C6CS00915H.
[38] Cançado LG, Monken VP, Campos JLE, Santos JCC, Backes C, Chachan H, et al. Science and metrology of defects in graphene using Raman spectroscopy. Carbon 2024;220:118801. https://doi.org/10.1016/j.carbon.2024.118801.

[39] Kim UJ, Furtado CA, Liu X, Chen G, Eklund PC. Raman and IR spectroscopy of chemically processed single walled carbon nanotubes. J Am Chem Soc 2005;127:15437–45. https://doi.org/10.1021/ja052951o.
[40] Stevie FA, Donley CL. Introduction to x-ray photoelectron spectroscopy. J Vac Sci Technol A 2020;38:063204. https://doi.org/10.1116/6.0000412.
[41] Jia Z, Chen T, Wang J, Wang J, Ni J, Li H, et al. Synthesis, characterization and tribological properties of Cu/reduced graphene oxide composites. Tribol Int 2015;88:17–24. https://doi.org/10.1016/j.triboint.2015.02.028.
[42] Raghupathy Y, Kamboj A, Rekha MY, Narasimha RNP, Srivastava C. Copper-graphene oxide composite coatings for corrosion protection of mild steel in 3.5% NaCl. Thin Solid Films 2017;636:107–15. https://doi.org/10.1016/j.tsf.2017.05.042.
[43] Ambrosi A, Chua CK, Latiff NM, Loo AH, Wong CHA, Eng AYS, et al. Graphene and its electrochemistry – an update. Chem Soc Rev 2016;45:2458–93. https://doi.org/10.1039/C6CS00136J.
[44] Pendashteh A, Mousavi MF, Rahmanifar MS. Fabrication of anchored copper oxide nanoparticles on graphene oxide nanosheets via an electrostatic coprecipitation and its application as supercapacitor. Electrochim Acta 2013;88:347–57. https://doi.org/10.1016/j.electacta.2012.10.088.
[45] Elgendy A, Nady H, El-Rabiei MM, Elhenawy AA. Understanding the adsorption performance of two glycine derivatives as novel and environmentally safe anti-corrosion agents for copper in chloride solutions: experimental, DFT, and MC studies. RSC Adv 2019;9:42120–31. https://doi.org/10.1039/C9RA08617J.
[46] Liu R, Han X, Wang F, Tan B, Zhang N, Li W, et al. Enhancing performance in copper corrosion inhibitors through molecular structural modifications: mechanisms, design, and future pathways. J Mol Liq 2024;394:123750. https://doi.org/10.1016/j.molliq.2023.123750.
[47] Jena G, Philip J. A review on recent advances in graphene oxide-based composite coatings for anticorrosion applications. Prog Org Coat 2022;173:107208. https://doi.org/10.1016/j.porgcoat.2022.107208.
[48] Cui G, Bi Z, Zhang R, Liu J, Yu X, Li Z. A comprehensive review on graphene-based anti-corrosive coatings. Chem Eng J 2019;373:104–21. https://doi.org/10.1016/j.cej.2019.05.034.
[49] Gravier J, Vignal V, Breton SB. Influence of residual stress, surface roughness and crystallographic texture induced by machining on the corrosion behaviour of copper in salt-fog atmosphere. Corros Sci 2012;61:162–70. https://doi.org/10.1016/j.corsci.2012.04.032.